



# Thermal annealing effect on phase evolution, physical properties of DC sputtered copper oxide thin films and transport behavior of ITO/CuO/Al Schottky diodes

K. A. Jagadish<sup>1</sup> · Dhananjaya Kekuda<sup>1</sup>

Received: 17 January 2024 / Accepted: 18 March 2024 / Published online: 16 April 2024  
© The Author(s) 2024

## Abstract

Herein, we report on the post-annealing temperature effect on the transport behavior of p-CuO/Al Schottky barrier diodes. In addition, the transformation of phase from Cu<sub>4</sub>O<sub>3</sub> to CuO phase was studied. Copper oxide thin films were grown on soda lime glass substrates, and post-annealing temperature's influence on the films' structural, chemical, morphological, and electrical characteristics was comprehensively examined. X-ray diffraction study revealed the development of polycrystalline tenorite phase (CuO) on annealing. Raman analysis also confirmed the formation of the tenorite phase (CuO) at higher annealing temperatures (400 °C and 500 °C). XPS study revealed the occurrence of the Cu<sub>4</sub>O<sub>3</sub> phase for room temperature deposited sample and CuO phase at the higher annealing temperature. Using current–voltage analysis, the Chueng model, and the thermoelectric emission model, the Schottky behavior between the metal and semiconductor were investigated. The fabricated diode showed a rectification ratio of 10<sup>3</sup> at ± 2 V, with the barrier height ranging from 0.84 to 1.12 eV due to different annealing treatments. The attributes of the power law were employed to elucidate space charge-limited conduction and the process of tunneling across the density of interface traps in p-CuO/Al Schottky diodes. This study provides valuable insights into the behavior of the p-CuO/Al Schottky junction, enhancing our understanding of its characteristics.

**Keywords** Thermal conversion · CuO · p-CuO/Al Schottky diode · XPS · Conduction mechanism · Annealing temperature

## 1 Introduction

The progress of semiconductor devices in recent years has been greatly aided by multifunctional thin films based on oxide materials. It is interesting to note that oxide semiconductors have adjustable bandgap/electrical conductivity and are optically transparent in the visible region. Moreover, they exhibit chemical stability and robust mechanical properties, which make them suitable for fabricating various devices. Gaining an understanding of the electrical, optical, and chemical composition of oxide semiconductors is crucial to their suitability for use in devices. The fundamental features of semiconductor materials, such as their ability to combine optical and electronic qualities, enable these

devices to have different functionalities. These attributes enable the interaction and control of photons, electrons, and holes utilizing various electronic environments and gadgets. The metal–semiconductor (MS) junction is a key component of contemporary electronic components, according to the majority of research [1]. Oxide semiconductors surpass traditional semiconductors like Si or Ge due to their distinctive physical properties, which can be easily tunable by manipulating growth parameters. Based on these processing conditions, certain oxide semiconductors, such as ZnO, CuO, NiO, FTO, exhibit favorable qualities for the devices [2–4]. They have a wide range of applications, including integrated circuits, solar cells, sensors, TFTs, photodetectors, field-effect transistors, and so on [3, 5–7]. Copper oxide shows good thermal stability, non-toxic behavior, good chemical stability, and less fabrication cost, and the relatively easy synthesis of copper oxide also makes it a desirable material for electronic and optoelectronic applications. As a well-known p-type semiconducting material, it has received a significant amount of attention. Cupric oxide (CuO) and cuprous oxide (Cu<sub>2</sub>O) have monoclinic and cubic

✉ Dhananjaya Kekuda  
dhaya.kekuda@manipal.edu

<sup>1</sup> Department of Physics, Manipal Institute of Technology, Manipal Academy of Higher Education, Manipal 576104, India

crystal structures, respectively, with optical energy band gap values of 1.3 eV to 2.1 eV and 2.0 eV to 2.6 eV [8]. Copper is found in both the oxidation states Cu(I) and Cu(II), as well as the fascinating intermediate phase paramelaconite  $\text{Cu}_4\text{O}_3$ , which may be written as  $\text{Cu}_2^+\text{Cu}_2^{2+}\text{O}_3$ ,  $\text{Cu}_4\text{O}_3$ , a tetragonal crystal structure with limited investigations, is known as paramelaconite and has a band gap of roughly 1.34 eV [9]. The oxide growth kinetics of all three oxides are heavily influenced by temperature, deposition rate, and oxygen pressure. Hence, a very narrow window of deposition parameters exists for creating a certain oxide phase and the differentiating variables are the growth parameters. Copper oxide thin films may be synthesized employing several deposition techniques, involving sol-gel dip coating [10], spray pyrolysis technique [11], hydrothermal method [12], rf sputtering [13], dc magnetron sputtering [14]. In this research work, dc magnetron sputtering is used since it is known to yield a better deposition rate, a lower substrate temperature during deposition and simple control of the film's stoichiometry, excellent adhesion to the substrate, and tunable morphology. Despite its importance, much about paramelaconite ( $\text{Cu}_4\text{O}_3$ ) is unknown. The transformation from  $\text{Cu}_4\text{O}_3$  to CuO and its characteristics are the focus of this paper. Since  $\text{Cu}_4\text{O}_3$  is a metastable phase, heat treatment affects its structural attributes. As a result, vacuum or air annealing can convert  $\text{Cu}_4\text{O}_3$  to CuO or  $\text{Cu}_2\text{O}$  [15]. Annealing is a post-processing approach for improving physical, optical, and electrical characteristics. D.S. Murali et al. [16] used high-temperature Raman spectroscopy to examine the impact of thermal treatment on  $\text{Cu}_4\text{O}_3$  films. They found that after annealing the films at 410 °C and 450 °C, the  $\text{Cu}_4\text{O}_3$  phase converted to the CuO phase. The metal-semiconductor junction serves as one of the frequently utilized rectifying contacts within the electronics sector [17]. Schottky diodes, which represent the most fundamental devices among MS contacts, hold substantial technological importance. CuO offers a high Schottky barrier height at metal-semiconductor junctions, which may hinder carrier injection and result in poor device performance, such as large leakage currents, low rectification ratio etc. Overcoming this high Schottky barrier height while keeping good electrical properties presents a substantial problem. CuO has limited carrier mobility and extended carrier recombination lifetimes, which can reduce the speed and efficiency of charge transfer in devices. Improving carrier mobility and decreasing recombination losses are crucial for improving device performance. Overcoming these constraints is critical in maximizing the potential of CuO Schottky diodes in a variety of electrical and optoelectronic applications. Therefore, an investigation into their electrical characteristics is highly intriguing. Furthermore, p-CuO/Al Schottky diodes are not well investigated. In this study, we fabricated and analyzed ITO/p-CuO/Al Schottky diodes, exploring their characteristics concerning

the post-annealing process applied to the sputtered p-CuO thin film.

## 2 Experimental details

### 2.1 Film deposition

Copper oxide thin films were deposited using reactive DC magnetron sputtering on soda lime glass substrates using a 2-inch. circular metallic copper target of 99.99% purity. The substrates were cleaned in an ultrasonicator individually with de-ionized water, acetone, and isopropyl alcohol. Following this, they were dried using Nitrogen gas and subjected to a UV-ozone treatment for ~ 10 min before being placed into a sputter chamber. Argon gas was introduced after the sputtering chamber was evacuated to  $1.6 \times 10^{-5}$  mbar. The metallic copper target was argon ion sputtered for 2 min before film deposition to eliminate surface adsorbates. During sputtering, the flow rates of argon gas (99.999% purity) and oxygen (99.999% purity) were kept at 5 sccm and 1 sccm, respectively. Oxygen acted as a reactive gas to get the desired oxide films. Mass flow controllers (Bronkhorst High-Tech, MFC) independently regulate both gas flow rates. At a partial pressure of 0.009 mbar, the deposition procedure was carried out, with a sputtering power of 30 W for 10 min. The substrate-to-target distance was kept constant at 7 cm. The films were air annealed in the temperature range 100–500 °C for 1 h. To fabricate the Schottky diode, we have utilized ITO coated glass substrate which served as the back electrode. Aluminum metal electrodes were applied to the samples through a thermal evaporation technique, using a shadow mask. Al electrode thickness was kept constant at 100 nm, with an evaporation rate of  $5 \text{ \AA s}^{-1}$ . Figure 1 displays a schematic representation of the device structure, while Fig. 2 illustrates the energy band diagram of the CuO/Al junction.

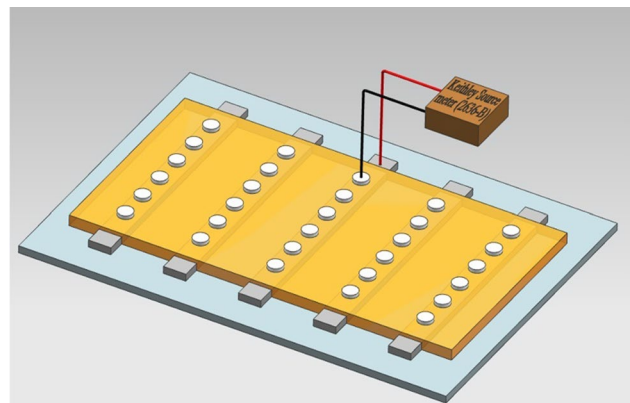


Fig. 1 Structural illustration of ITO/p-CuO/Al Schottky diode

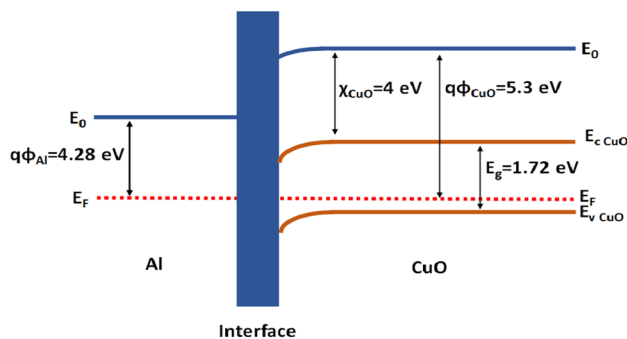


Fig. 2 Schematic energy band alignment of ITO/p-CuO/Al Schottky diodes

## 2.2 Film characterizations

The thickness of the films was measured using a BRUKER Dektak XT stylus Profilometer and was determined to be 310 nm. XRD (3rd gen Empyrean, Malvern Panalytical multipurpose diffractometer) ( $\text{Cu K}\alpha$ ,  $\lambda = 1.54 \text{ \AA}$ ) was employed to study the film crystal structure with patterns taken in the  $2\theta$  range  $20^\circ$ – $80^\circ$ . The structural composition of the films was examined by a Raman spectrometer (Compact Raman spectrometer, *Renishaw*) using a wavelength for excitation at 532 nm. AFM (Flex-axiom AFM) was utilized to evaluate the surface morphology and roughness of the films. X-ray photoelectron spectroscopy PES-BL14 (1.5 T bending magnet) was used to determine the chemical composition and electronic state of the elements present in the films. Electrical measurements of sputtered copper oxide films were carried out at ambient temperature using a Hall effect instrument (3706 A-Switch) in a magnetic field of 0.60 T. Ultimately, a Keithley (2636-B source meter) semiconductor characterization unit was used to characterize the transport properties of the fabricated Schottky diodes.

## 3 Results and discussion

### 3.1 Structural analysis

X-ray diffraction (XRD) studies were performed to investigate alterations in the structural characteristics of Copper Oxide films due to the thermal annealing and the corresponding spectra were recorded in the  $2\theta$  range  $20^\circ$ – $80^\circ$ . The polycrystalline nature of the grown films is evident from the Fig. 3. Tenorite ( $\text{CuO}$ ), cuprite ( $\text{Cu}_2\text{O}$ ), and paramelaconite ( $\text{Cu}_4\text{O}_3$ ) are the common phases in which copper oxide may be found. The as-deposited sample's XRD traces showed peaks with diffraction angles ( $2\theta$ ) of  $30.62^\circ$ ,  $35.7^\circ$ , and  $63.9^\circ$ . The paramelaconite ( $\text{Cu}_4\text{O}_3$ ) phase of copper oxide was demonstrated by these peaks, which were attributed to the Bragg reflections

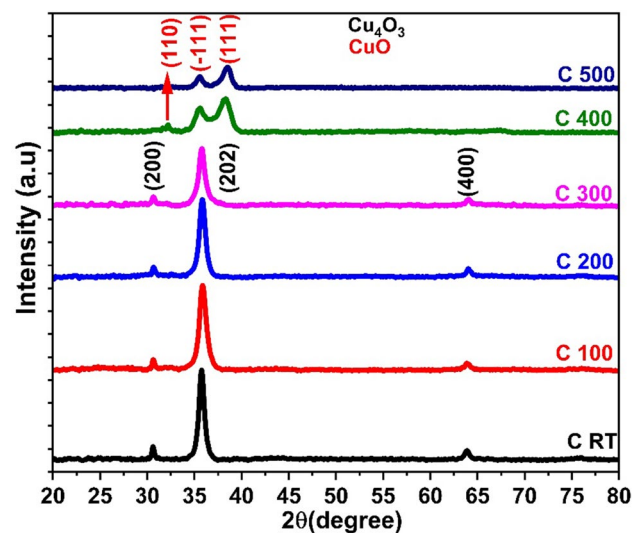


Fig. 3 XRD pattern of as-deposited and annealed Copper Oxide thin films at different temperatures

(200), (202), and (400) (JCPDS card: 01-071-6397). With a rise in annealing temperature, the diffraction peak intensities fall, which lowers the crystallinity of the films. The peak intensity corresponding to (200), (202), and (400) of the annealed  $\text{Cu}_4\text{O}_3$  films significantly reduced with an increase in annealing temperature, reaching a minimum at  $500^\circ\text{C}$ . Peaks ascribed to the first plane decreased and a modest peak shift was noticed, which may have been caused by compositional changes and the conversion of one phase to another. Except for the  $400^\circ\text{C}$  and  $500^\circ\text{C}$  annealed films, all films with 141/ and (141) space group had the paramelaconite  $\text{Cu}_4\text{O}_3$  phase, with a tetragonal crystal structure. At  $400^\circ\text{C}$ , the  $\text{CuO}$ -related peaks appeared at  $2\theta = 32.21^\circ$ ,  $35.60^\circ$ , and  $38.31^\circ$ , which are related to the (110), ( $-111$ ) and (111) planes, respectively. Copper oxide was found to be in the  $\text{Cu}_4\text{O}_3$  form in samples that were annealed at  $100^\circ\text{C}$ ,  $200^\circ\text{C}$ , and  $300^\circ\text{C}$ . At  $400^\circ\text{C}$ , the  $\text{CuO}$  form with vanished  $\text{Cu}_4\text{O}_3$  peaks was seen.  $\text{Cu}_4\text{O}_3$  had completely changed to the  $\text{CuO}$  phase when the annealing temperature was raised to  $400^\circ\text{C}$ , as shown by the XRD. At  $500^\circ\text{C}$ , the  $\text{CuO}$  (110) diffraction peak vanished, leaving only the  $\text{CuO}$  ( $-111$ ) and (111) diffraction peaks. The possibility of oxygen diffusion into the films leads to the transformation of  $\text{Cu}_4\text{O}_3$  into  $\text{CuO}$ .  $\text{Cu}_4\text{O}_3$  reacts with  $\text{O}_2$  to generate the  $\text{CuO}$  phase through the following reaction:  $2 \text{Cu}_4\text{O}_3 + \text{O}_2 \rightarrow 8 \text{CuO}$ . The XRD results demonstrate that temperature-controlled synthesis of pure  $\text{Cu}_4\text{O}_3$  and pure  $\text{CuO}$  films is possible. The film structure does indeed change during annealing, according to XRD studies (Fig. 3). No diffraction peaks of the  $\text{Cu}_4\text{O}_3$  phase can be identified for films that have been annealed at  $400^\circ\text{C}$  and  $500^\circ\text{C}$ ; only tenorite peaks can be seen. The  $\text{Cu}_4\text{O}_3$  is subsequently fully oxidized to  $\text{CuO}$  at annealing temperatures exceeding  $400^\circ\text{C}$ . This shows that paramelaconite films react

in an oxidizing environment similar to  $\text{Cu}_2\text{O}$  [18]. Furthermore, the paramelaconite phase possesses a greater crystal size ( $\sim 18.0$  nm) than the tenorite phase (estimated at 7.6 nm). As a result, the crystallite size falls during film oxidation. This result contradicts the findings of Li et al. [19] where no grain size change was observed during the oxidation of  $\text{Cu}_4\text{O}_3$  to  $\text{CuO}$ . Furthermore, from the Debye-Scherrer relation [16], the crystallite sizes corresponding to the primary peaks were computed as 18.0 nm, 15.0 nm, 14.5 nm, 14.6 nm, 10.7 nm, and 7.4 nm, respectively, for the as-deposited, 100 °C, 200 °C, 300 °C, 400 °C and 500 °C annealed films. The poor growth rate of copper oxide films resulted in a comparatively tiny crystallite size at elevated annealing temperatures.

$$D = \frac{0.9 \times \lambda}{\beta \cos \theta} \quad (1)$$

Here  $D$  represents the crystallite size,  $\beta$  is FWHM and  $\lambda$  is the incident X-ray wavelength [15].

The diffraction peaks of all  $\text{Cu}_4\text{O}_3$  and  $\text{CuO}$  films coordinated the Tetragonal  $\text{Cu}_4\text{O}_3$  and monoclinic  $\text{CuO}$  standard data card (Standard data card: 01-083-1665 and 00-041-0254).

The density of defects in the films, denoted by the dislocation density, was determined by applying the Williamson-Smallman relation. The presence of strain and dislocation density might impact the device performance, thus the lattice strain and dislocation density were evaluated in the current work utilizing the relation [14].

$$\delta = \frac{1}{D^2} \quad (2)$$

$D$  is crystallite size and is dislocation density. Lattice strain can be calculated using the following equation:

$$\epsilon = \frac{\beta \cos \theta}{4} \quad (3)$$

$\beta$  in radians is the FWHM corresponding to the plane. Following post-annealing, there was an increase in dislocation

density and lattice strain, indicating a decrease in crystallinity due to heat treatment.

The number of crystallites per unit area ( $N$ ) was obtained using: [14].

$$N = \frac{t}{D^3}, \quad (4)$$

where  $t$  is the thickness of the film. The number of crystallites per unit area increased upon post-annealing due to the reduction in crystallite size with annealing temperature. A higher number of smaller crystallites per unit area typically suggests a finer grain size distribution. The calculated values are shown in Table 1.

### 3.2 Raman spectroscopy

To comprehend the structural details better and to establish a distinction between the various  $\text{Cu}_4\text{O}_3$  and  $\text{CuO}$  phases that are present in copper oxide films, Raman spectroscopy was conducted in the 100–2000  $\text{cm}^{-1}$  spectral region. The copper (II) oxide ( $\text{CuO}$ ), which has 2 molecules per primitive cell, belongs to the  $C_2^6h$  space group. There are 6 IR active modes ( $3A_u + 3B_u$ ), 3 acoustic modes ( $A_u + 2B_u$ ) and only 3 are Raman active modes ( $A_g + 2B_g$ ) out of the 9 zone-center optical phonon modes with symmetry  $4A_u + 5B_u + A_g + 2B_g$  [5]. According to the paramelaconite ( $\text{Cu}_4\text{O}_3$ ) structural group theory, there are 42 symmetrical vibrational modes “ $3E_g + A_{1g} + 2B_{1g} + 9E_u + 6A_{2u} + 5B_{2u} + 2B_{1u} + 2A_{1u}$ ”, out of which 9 ( $3E_g + A_{1g} + 2B_{1g}$ ) modes are Raman active, 21 are IR active ( $A_{2u}$  and  $E_u$ ), and 9 are silent ( $A_{1u}$ ,  $B_{1u}$ , and  $B_{2u}$ ) [9, 20, 21]. Figure 4 presents the Raman spectra of the films. The Raman spectrum of thin film deposited at room temperature shows the characteristic peaks of  $\text{CuO}$  at 282  $\text{cm}^{-1}$ , 619  $\text{cm}^{-1}$ , 1077  $\text{cm}^{-1}$ , and  $\text{Cu}_4\text{O}_3$  peaks at 532  $\text{cm}^{-1}$  [13, 21]. The strong peak at 532  $\text{cm}^{-1}$  was caused by the  $\text{Cu}_4\text{O}_3$  crystals’  $A_{1g}$  Raman-allowed mode; the faint peak at 282  $\text{cm}^{-1}$  is attributed to  $A_g$ ; 619  $\text{cm}^{-1}$  belongs to the  $B_g$  mode; and 1077  $\text{cm}^{-1}$  refers to the  $2B_g$  mode, which is a Cu–O stretching mode. Additionally, Irwin et al. [22]

**Table 1** Structural and electrical characteristics of copper oxide thin films annealed at different temperatures

Sample	Phase	Average crystallite size (nm)	Dislocation density ( $\delta$ ) $\times 10^{15}$ ( $\text{m}^{-2}$ )	Lattice strain ( $\epsilon$ ) $\times 10^{-3}$	Crystallites per unit area ( $N$ ) ( $\text{m}^{-2}$ ) $\times 10^{17}$	Resistivity ( $\Omega\text{-cm}$ ) $\times 10^2$	Hall mobility ( $\text{cm}^2 \text{V}^{-1} \text{s}^{-1}$ )	Carrier concentration ( $\text{cm}^{-3}$ ) $\times 10^{16}$
C RT	$\text{Cu}_4\text{O}_3$	18	4.02	6.1	0.53	23.02	0.91	0.3
C 100	$\text{Cu}_4\text{O}_3$	15	6.11	7.51	0.92	25.52	1.32	0.19
C 200	$\text{Cu}_4\text{O}_3$	14.5	5.46	7.34	1.02	12.83	2.48	0.2
C 300	$\text{Cu}_4\text{O}_3$	14.6	5.35	7.33	1	16.64	1.69	0.22
C 400	$\text{CuO}$	10.7	21.51	14.88	2.56	4.15	1.71	0.88
C 500	$\text{CuO}$	7.4	18.53	14.84	7.76	0.44	2.12	6.84



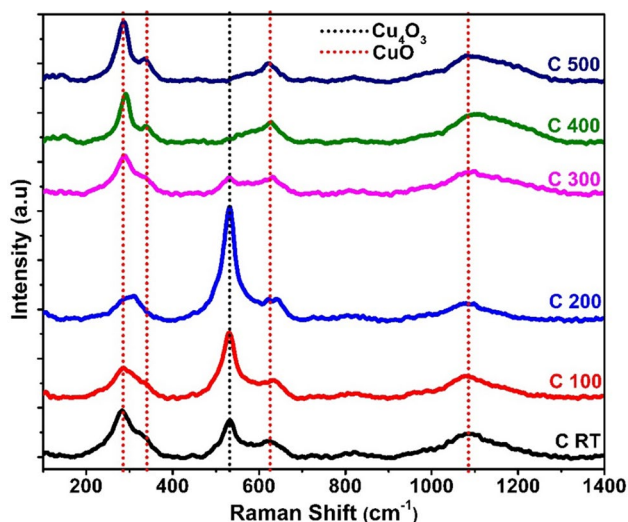


**Fig. 4** Raman spectrum of copper oxide thin films annealed at different temperatures

also noticed a noticeable peak at around  $1077\text{ cm}^{-1}$ , which they linked to the scattering of two phonons in CuO. The Raman spectrum of copper oxide films annealed till  $300\text{ }^{\circ}\text{C}$  shows the mixed phase of CuO and  $\text{Cu}_4\text{O}_3$ , the film annealed at  $400\text{ }^{\circ}\text{C}$  shows an additional shift at  $339\text{ cm}^{-1}$  which corresponds to the  $\text{B}_g$  mode of CuO, and the shift at  $532\text{ cm}^{-1}$  disappeared and the film shows all the shifts corresponds to CuO phase. In addition to the typical CuO peaks, the copper oxide film's spectra show a strong peak at  $532\text{ cm}^{-1}$ , which is associated with the  $\text{Cu}_4\text{O}_3$  phase's  $\text{A}_g^1$  mode [16]. This suggests that the CuO phase may develop preferentially in

films that have been annealed over  $400\text{ }^{\circ}\text{C}$ . The oxidation of the unstable  $\text{Cu}_4\text{O}_3$  phase may be the cause of the CuO peak. These results support our XRD results and show that raising the annealing temperature from  $100\text{ }^{\circ}\text{C}$  to  $500\text{ }^{\circ}\text{C}$  causes the copper oxide films  $\text{Cu}_4\text{O}_3$  phase to transform into CuO. The synthesized thin films are absent from any  $\text{Cu}_2\text{O}$  modes.

### 3.3 Morphological study

Atomic force microscopy (AFM) was utilized to assess both the surface morphology and the roughness of the films. Figure 5a–f illustrates 3-D AFM images (of  $2 \times 2\text{ }\mu\text{m}^2$ ) for the as-grown, and annealed films ( $100\text{--}500\text{ }^{\circ}\text{C}$ ). After annealing, there is a clear indication of the changes in the surface topography of the films. The thin film in its initial state consists of extremely small grains and exhibited a smooth surface with a root-mean-square (RMS) roughness of  $3.93\text{ nm}$ . As the post-deposition annealing temperature increased, the average crystallite size decreased according to XRD analysis, and the roughness increased with maximum roughness ( $7.99\text{ nm}$ ) observed for  $500\text{ }^{\circ}\text{C}$  annealed film. Smaller crystallites may also experience higher internal strain or stress due to the boundaries between them. This strain can contribute to the distortion of the lattice structure, resulting in surface roughness. Consequently, an increase in film roughness is observed with an increase in lattice strain. This finding is consistent with the XRD results. Figure 3c–f shows the creation of particle clusters, which were found to be configurations of collapsing grains with a pattern resembling a polycrystalline film. As a result of the increased annealing temperature, the roughness increased. This behavior is

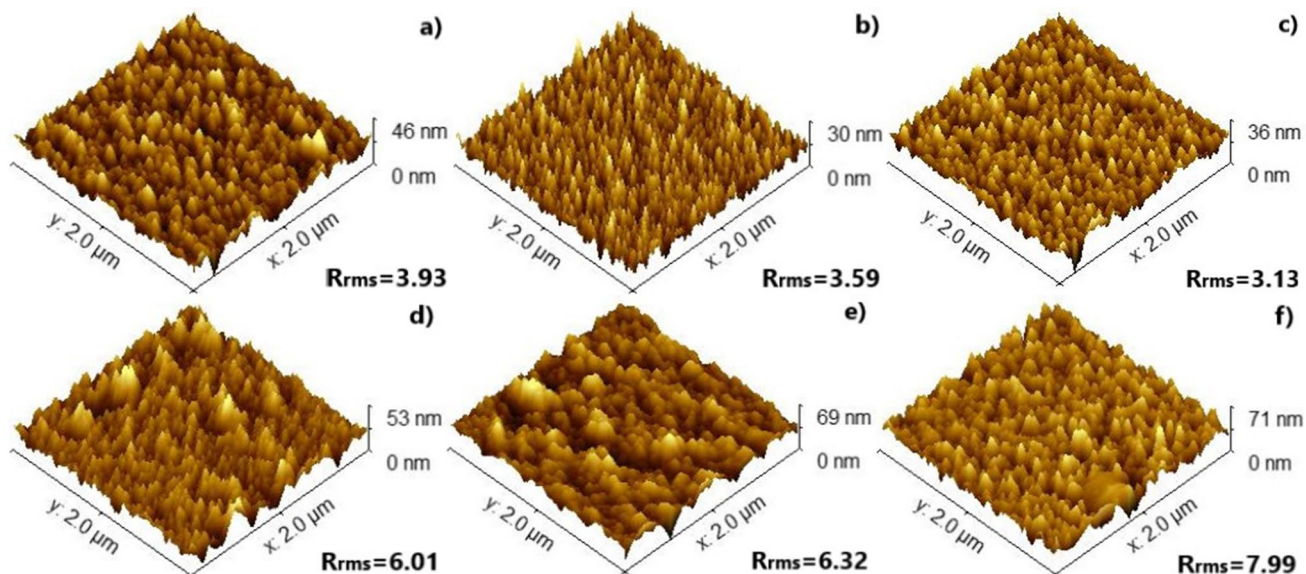


**Fig. 5** 3D AFM images of (a) as-deposited and annealed thin film at different temperatures of (b)  $100\text{ }^{\circ}\text{C}$ , (c)  $200\text{ }^{\circ}\text{C}$ , (d)  $300\text{ }^{\circ}\text{C}$ , (e)  $400\text{ }^{\circ}\text{C}$  and (f)  $500\text{ }^{\circ}\text{C}$

consistent with prior research by Park et al. [23]. The variation in surface morphologies is related to the changes in copper oxide phase [15].

### 3.4 Chemical analysis

XPS analysis was utilized to explore the structure and surface chemical composition of the copper oxide thin films for varied annealing temperatures. The wide spectra, Cu 2p, and O 1s spectra were plotted after charging effect correction (carbon correction) for the binding energy of C 1s at 284.80 eV. After adjusting for carbon, elemental mapping through the survey spectrum was conducted for copper oxide thin films in their as-deposited state as well as the samples annealed at 400 °C and 500 °C. The outcomes are depicted in Fig. 6. They contain Cu 2s, Cu 2p, Cu 3s, and O 1s core level peaks, and the sole adventitious impurity found on the surface of the films was carbon. No foreign elements are observed in broad spectra, indicating that the formed film had the appropriate Copper oxide composition during the sputtering procedure. To determine the chemical composition, the background of the high-resolution Cu 2p and O1s XPS spectra was corrected using a Shirley type of background and deconvoluted using a mixed Gaussian/Lorentzian function. The core level spectra for Cu 2p and O1s are shown in Fig. 7a–f. The extracted chemical states and percentage concentrations from the deconvoluted peaks are tabulated in Table 2. The Cu2p core level spectra of the as-deposited film (Fig. 7a) surface reveal a doublet at 931.42 eV and 951.26 eV for Cu2p<sub>3/2</sub> and Cu2p<sub>1/2</sub>, respectively [24]. The Cu2p<sub>3/2</sub> peak profiles were fitted with two contributions ascribed to CuO (931.42 eV) and Cu<sub>2</sub>O (932.84 eV)

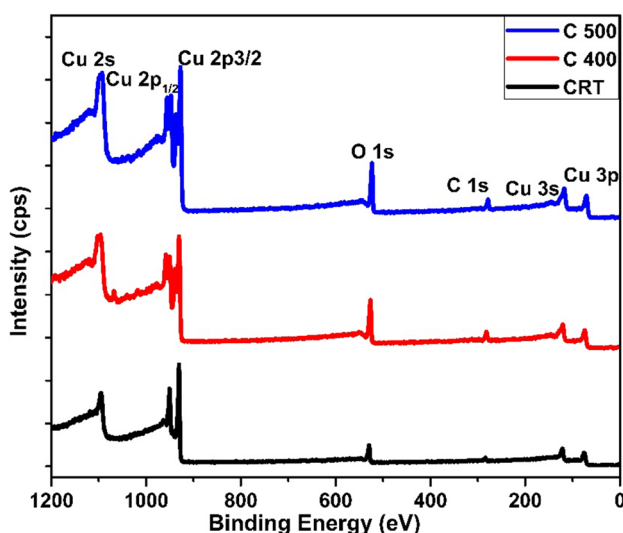


**Fig. 6** XPS wide spectra of copper oxide thin film deposited and annealed at 400 °C and 500 °C

[25]. Similarly, The Cu2p<sub>1/2</sub> peak profiles were fitted with two contributions ascribed to CuO (952.96 eV), and Cu<sub>2</sub>O (951.26 eV) [26]. The lack of the signal at 918.30 eV suggests that the samples do not contain Cu metal [24]. Depending on the binding energy of the sample, peaks, and oxidation states for each sample were determined, as shown in Fig. 7. The approximated chemical compositions are detailed in Table 2.

The deconvoluted XPS Cu 2p and O 1s spectra for 400 °C and 500 °C annealed copper oxide films are shown in Fig. 7c–f. Both samples' Cu 2p energy levels consisted of the main characteristic peaks for Cu 2p<sub>1/2</sub> and Cu 2p<sub>3/2</sub> at 953.32 eV and 933.06 eV, respectively [11]. The presence of peaks at 940.58 eV and 943.04 eV signifies Cu<sup>2+</sup> in its ground state, displaying the d<sup>9</sup> configuration. Additionally, satellite peaks are observed at ~ 7 eV and 10 eV above the primary Cu 2p peak [27]. Peak separation, or spin–orbit splitting, between Cu 2p<sub>1/2</sub> and Cu 2p<sub>3/2</sub>, was discovered to be about 20 eV and was comparable with the previously reported data [26]. The satellite peaks located on the higher binding energy side of the core level Cu 2p XPS data are recognized as carrying properties associated with the CuO phase, owing to numerous excitations present in copper oxides. Consequently, both samples' Cu 2p XPS spectra showed substantial shake-up satellite structures, which suggested the presence of CuO. The appearance of the satellite peaks in the spectra could be attributed to the copper metal 3d → 4s shake-up transition or the transfer of charge from the ligand orbital to the metal orbital [14]. However, as the cuprous phase contains a fully occupied d<sup>10</sup> orbital configuration, the transfer of charge into the d shell is not possible. As a result, satellite peaks are typically missing in the Cu<sub>2</sub>O phase [28]. The primary peak and satellite peaks' binding energies were examined to determine the existence of cupric oxide in the film. The quantity of cuprous oxide phase (Cu<sup>2+</sup>) and cupric oxide phase (Cu<sup>+</sup>) present in the film may be determined by calculating the precise area of the main peak and satellite peak. The relationship shown below can be used to determine the proportion of Cu<sup>2+</sup> and Cu<sup>+</sup> [29],

$$\% \text{ of } Cu^{2+} = \frac{A}{A + B}. \quad (5)$$

A encompasses the area of the Cu<sup>2+</sup> 2p<sub>3/2</sub> peak along with the zones corresponding to the satellite 2p<sub>3/2</sub> peaks. B covers the Cu<sup>+</sup> 2p<sub>3/2</sub> peak region. The primary 2p<sub>3/2</sub> peak in the as-deposited film is a result of contributions from both Cu<sup>2+</sup> and Cu<sup>+</sup>. Consequently, the amount of Cu<sup>2+</sup> discovered in the deposited sample is 51.94%, indicating that the film surface includes almost equal amounts of Cu<sup>2+</sup> and Cu<sup>+</sup>. This suggests that the sample contains a combination of Cu<sup>2+</sup> and Cu<sup>+</sup> (almost equal quantities), confirming the paramelaconite phase. While no peaks corresponding to

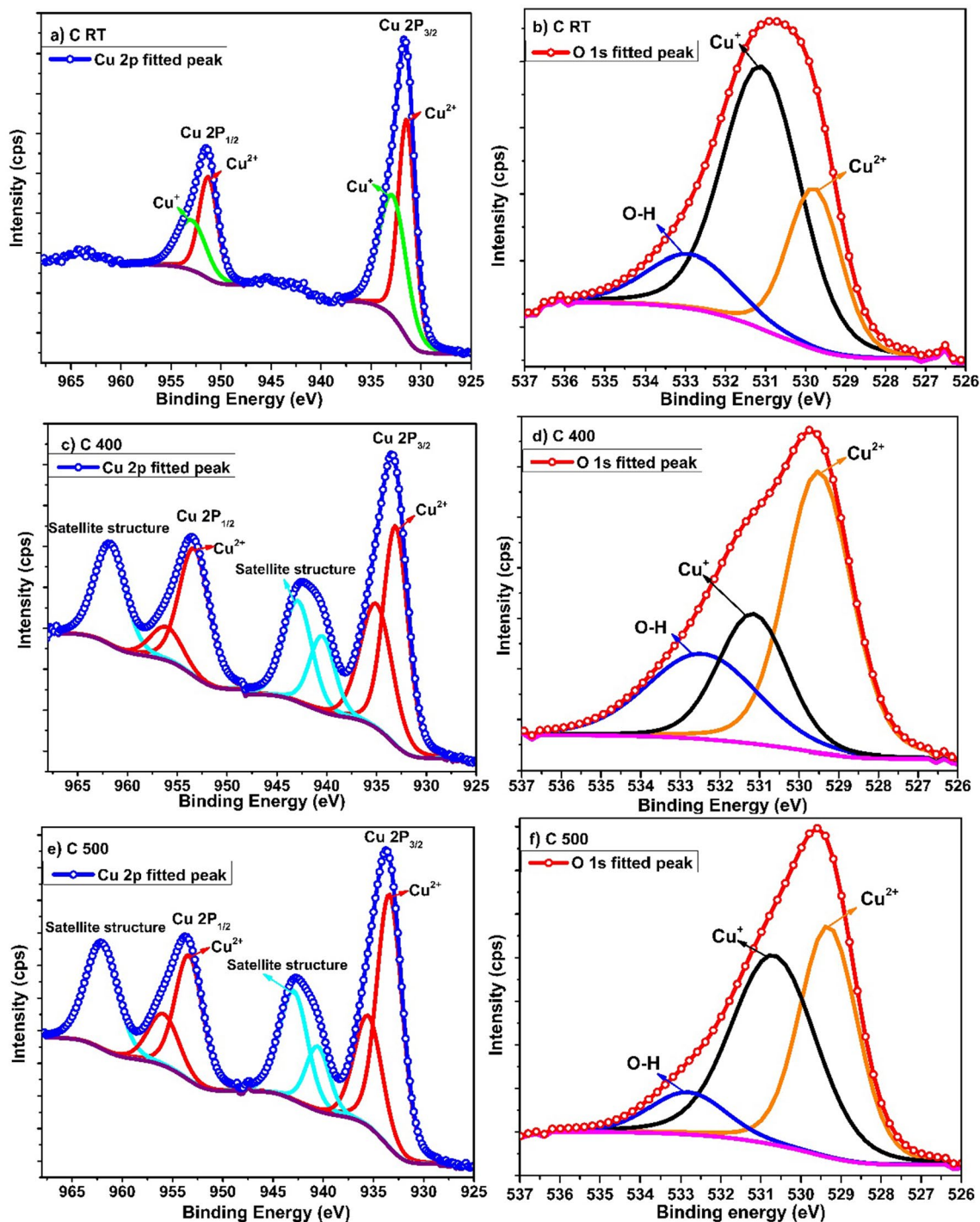


**Fig. 7** Deconvoluted Cu 2p (a, c, e) and O 1s (b, d, f) XPS core level spectra belonging to as deposited, 400 °C and 500 °C annealed copper oxide thin films

Cu<sup>+</sup> are found in films annealed at 400 °C and 500 °C, the film is transformed to CuO phase by post-annealing above 400 °C. The integrated regions of the O1s and Cu(2p<sub>3/2</sub>) peaks were used to compute the overall Cu:O ratio for all samples. The Cu:O ratio was calculated using the following formula [30].

$$\left(\frac{Cu}{O}\right)_{stoch} = \left(\frac{I_{Cu}}{I_O}\right) \left(\frac{S_O}{S_{Cu}}\right) \left[\frac{1 - \exp(-1/\cos 45^\circ \lambda_{Cu})}{1 - \exp(-1/\cos 45^\circ \lambda_O)}\right], \tag{6}$$

where  $I_x$  and  $S_x$  are integrated areas and sensitivity factors of corresponding elements. The inelastic mean free path

**Table 2** Data extracted from XPS spectra of as-deposited, 400 °C, and 500 °C annealed films

Sample	Element	Peak assignment	Binding energy (eV)	FWHM	% concentration	Cu:O	CuO: Cu <sub>2</sub> O
C RT	Cu 2p	Cu <sup>2+</sup>	931.42	1.99	35.16	1.5:1	51.94: 48.06
		Cu <sup>+</sup>	932.84	3.29	32.53		
		Cu <sup>+</sup>	951.26	2.2	18.22		
		Cu <sup>2+</sup>	952.96	3.46	14.09		
	O 1s	Cu <sup>2+</sup>	529.78	1.56	22.38		
		Cu <sup>+</sup>	531.09	2.36	57.42		
		Adsorbed oxygen	533.02	3.47	20.19		
C 400	Cu 2p	Cu <sup>2+</sup>	933.06	2.94	23.32	0.7:1	–
		Cu <sup>2+</sup>	935.03	3.89	18.17		
		Satellite peak	940.58	3.16	9.63		
		Satellite peak	943.04	3.27	11.51		
		Cu <sup>2+</sup>	953.32	3.4	15.43		
		Cu <sup>2+</sup>	955.78	3.78	6.28		
		Satellite peak	961.8	4.09	15.66		
		O 1s	Cu <sup>2+</sup>	529.41	1.84		
	Cu <sup>+</sup>		531.09	2.92	53.75		
	Adsorbed oxygen		533.52	2.52	8.16		
	C 500	Cu 2p	Cu <sup>2+</sup>	933.27	2.9		
Cu <sup>2+</sup>			935.23	3.5	17.38		
Satellite peak			940.86	3.12	9.52		
Satellite peak			943.21	3.01	10.75		
Cu <sup>2+</sup>			953.23	3.15	13.38		
Cu <sup>2+</sup>			955.54	3.98	9.18		
Satellite peak			962.04	3.79	14.88		
O 1s		Cu <sup>2+</sup>	529.36	1.82	48.26		
		Cu <sup>+</sup>	530.81	2.28	38.64		
		Adsorbed oxygen	532.74	2.59	13.09		

(IMFP) ( $\lambda_x$ ) for copper and oxygen were calculated using the formula below:

$$\lambda_x = A_1 E^{-2} + B_1 E^{1/2}, \quad (7)$$

where E is the measured electron's kinetic energy (eV),  $A_1$  and  $B_1$  are empirically fitted constants of 538 and 0.210, and  $\lambda_x$  is in monolayers. The total Cu:O ratio for the deposited film was determined using these formulae to be 1.5:1. This ratio is greater than the predicted composition (1.33:1) for this structure, even though it is still within the acceptable ranges of CuO and Cu<sub>2</sub>O.

Figure 7b, d, f shows O 1s core level spectra for as-deposited, 400 °C and 500 °C annealed samples. The highest intensity peak, situated at 531.09 eV, was identified which is believed to be originating from the defective oxide Cu<sub>2</sub>O (Cu<sup>+</sup>). Meanwhile, the peak at 529.78 eV is linked to the regular O<sup>2-</sup> interacting with Cu<sup>2+</sup> to create the Cu–O bond. The presence of the adsorbed O<sub>2</sub> element on the deposited copper oxide surface layer is denoted by the peak at

533.02 eV [11]. The findings are consistent with a previously published paper by Biesinger et al. [29]. While the shape of the O1s core level spectra of the annealed thin films varied, it can still be deconvoluted into three components associated with adsorbed oxygen, Cu<sub>2</sub>O (Cu<sup>+</sup>) defective oxide, and CuO (Cu<sup>2+</sup>) lattice oxides at respective energies of 533.52 eV, 531.09 eV, and 529.41 eV [31].

### 3.5 Electrical study

On the identical copper oxide films formed under ideal deposition conditions at ambient temperature and air annealed at different temperatures, electrical resistivity, and Hall mobility ( $\mu$ ) were measured. A set of 5 samples annealed at different temperatures was subjected to Hall measurement. The van der Pauw approach was utilized to make the above measurements with appropriate ohmic connections, and all the films have shown p-type conductivity. Copper oxide films' p-type behavior was previously attributed to the existence of Cu vacancies. The resistivity of the as-deposited film was



$2 \times 10^2 \Omega\text{-cm}$ , and it decreased to  $0.44 \times 10^2 \Omega\text{-cm}$  for films annealed at  $500^\circ\text{C}$ . The development of Cu vacancies in the  $\text{Cu}_x\text{O}$  layer causes reduced resistivity after annealing. The grain boundary scattering increases with decreasing crystallite size and influences copper oxide thin films' resistivity. This might be owing to the lower  $\text{Cu}^+$  ions over  $\text{Cu}^{2+}$  ions and these findings are consistent with XRD. Moreover, the charge carrier mobility and carrier concentration increase with annealing temperature. The film annealed at  $500^\circ\text{C}$  was found to have a maximum carrier concentration of  $6.84 \times 10^{16} \text{cm}^{-3}$ . This investigation, as presented in Table 1, showed that the presence of copper vacancies in the  $\text{Cu}_x\text{O}$  films resulted in a guaranteed rise in carrier concentration. Further, the carrier mobility has continuously increased to  $2.48 \text{cm}^2 \text{V}^{-1} \text{s}^{-1}$  with increased annealing temperature up to  $200^\circ\text{C}$ , and subsequently, the mobility values marginally decreased to  $2.12 \text{cm}^2 \text{V}^{-1} \text{s}^{-1}$  with a further rise in annealing temperature. Because of colloidal energy loss with oxygen during the sputtering, the carrier mobility has decreased [32].

### 3.6 Current–voltage characteristics for ITO/p-CuO/Al Schottky diode

Figure 8a, b depicts the current–voltage plot and the power law behavior of p-CuO/Al Schottky diodes measured under dark conditions at ambient temperature. The device's bias voltage ranged from  $-2$  to  $+2$  V. On a p-type semiconductor, aluminum with a work function of  $4.28 \text{eV}$  was chosen as Schottky contact. Figure 1 presents a schematic representation of the ITO/p-CuO/Al Schottky diode structure. It is observed that following the annealing procedure, all the devices exhibited a rectifying behavior. The exponential rise in forward current coupled with a slight reliance on reverse voltages is a typical trait of a rectifying junction. Figure 8 depicts the

rectifying behavior seen in this study. The junctions of CuO thin films annealed at various temperatures were studied. For all devices in the dark, the rectification ratio was in the range of  $10^2\text{--}10^3$ . The rectification is caused by the formation of inherent defects within the CuO thin films and at the metal–semiconductor interface. Due to the narrowing of energy bands at low forward bias, there is a substantial increase in voltage–current density, resulting in the dominance of a space charge-limited current (SCLC) mechanism [4]. Many factors may influence Schottky diode properties, which include interfaces, sputtering conditions, copper stoichiometry, and oxygen composition. The thermionic emission model (TE) was used to obtain heterojunction characteristics for instance saturation current ( $I_0$ ), ideality factor ( $\eta$ ), and the barrier height ( $\phi_B$ ) from the I–V graph. The TE model states that the following equation may be used to represent the I–V relation of heterojunction.

$$I = I_0(e^{\frac{qV}{\eta kT}} - 1), \tag{8}$$

$I_0$ ,  $V$ ,  $\eta$ ,  $k$ , and  $T$  are recognized in this context to denote the following:  $I_0$  as saturation current,  $V$  is applied voltage,  $\eta$ —ideality factor,  $k$ —Boltzmann's constant, and  $T$ —the temperature in kelvin, often referring to room temperature. The saturation current  $I_0$  is given by the relation:

$$I_0 = AA^*T^2 e^{-q\phi_B/kT}, \tag{9}$$

where  $A$  is the contact area ( $4.42 \times 10^{-3} \text{cm}^2$ ),  $A^* = 949.36 \text{A cm}^{-2} \text{K}^{-2}$  is Richardson's constant for CuO and  $\phi_B$  represents the barrier height of the CuO/Al interface at zero bias [33]. Equation (8), can be modified as:

$$\ln(I) = \frac{qV}{\eta kT} + \ln(I_0). \tag{10}$$

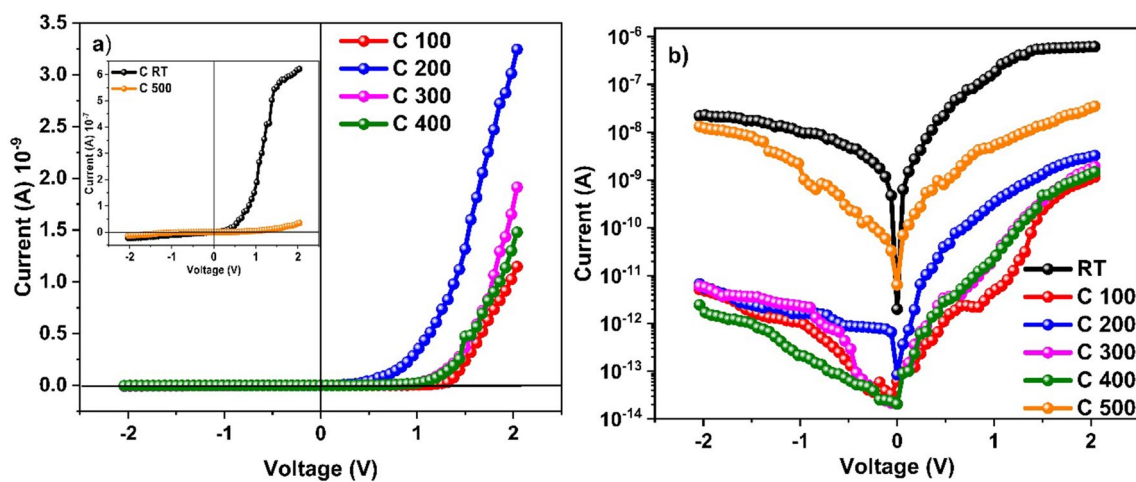


Fig. 8 I–V characteristics of the device, (a) at linear scale, and (b) at log scale

The slope of the linear segment in the forward region and the intercept from the semi-logarithmic plot of the I-V characteristics were used to calculate the ideality factor ( $\eta$ ) and barrier height ( $\phi_B$ ). The barrier height was computed utilizing Eq. (9), and the outcomes are presented in Table 3. The value of the ideality factor ( $\eta$ ), close to one in an ideal diode, determines the quality of the constructed diode. The ideality factor  $\eta$  relates to tunneling current and fluctuates between 1 and 2, according to the semiconductor diode theory;  $n > 2$  indicates the presence of leakage current; if  $n = 2$  is the result of the generation and recombination current processes [34]. Table 3 describes the Schottky diode parameters. After annealing, significant changes in the ideality variables were noted. It might be caused by variations in the inhomogeneities in barrier heights, and the recombination of surface/interface defects [6]. Careful examination of I-V curves demonstrates the device's progressive increase in threshold voltage ( $V_T$ ) due to annealing. The increase in  $V_T$  might be attributable to two factors: (i) increased impurity diffusion when subjected to higher annealing conditions, resulting in an expansion of the depletion zone, and (ii) the offsetting of  $O_2$  vacancies at the junction following annealing [35]. The room temperature device has a leakage current of  $2.17 \times 10^{-8}$  A and a rectification ratio of  $2.85 \times 10^1$  measured in the voltage range of  $-2$  V to  $+2$  V. The leakage current gradually decreased following annealing treatment (Fig. 8b). For the sample treated at  $400^\circ\text{C}$ , the improved rectification ratio was around  $6.04 \times 10^2$ , with a decreased leakage current of  $2.44 \times 10^{-12}$  A. This increase in electrical characteristics might be attributed to lower oxygen-related trap densities after annealing [36]. While producing the device, factors like material composition, thickness, structure, and interface play a crucial role in influencing both the leakage current and series resistance ( $R_s$ ). Any defects in the CuO films can significantly impact these characteristics. Diodes, typically, don't follow a linear I-V curve, and this behavior is heavily influenced by the series resistance ( $R_s$ ), a pivotal parameter affecting device performance.

$$I = I_0(e^{\frac{q(V-IR_s)}{\eta kT}} - 1). \tag{11}$$

On differentiating the Eq. (14) concerning I, which gives,

$$\frac{dV}{d(\ln I)} = IR_s + \frac{\eta kT}{q}. \tag{12}$$

The equation above represents a linear equation form. Accordingly, Cheung's functions are used to predict the  $\phi_B$ ,  $\eta$ , and  $R_s$  of the MS (metal–semiconductor) junctions within the non-linear section of forward-bias I–V curves. By plotting  $dV/d(\ln I)$  against I, we can determine the slope and intercept, thereby obtaining the  $R_s$  and  $\eta$ . Similarly, plotting  $H(I)$  against I will also yield both  $R_s$  and  $\phi_B$  according to the provided equation.

$$H(I) = IR_s + \eta\Phi_B, \tag{13}$$

where,

$$\Phi_B = \frac{H(I) - I(R_s)}{\eta}. \tag{14}$$

$$H(I) = V - \frac{\eta kT}{q} \ln\left(\frac{I}{AA^*T^2}\right). \tag{15}$$

Figure 9 displays graphs representing  $dV/d(\ln I)$  and  $H(I)$  for all samples under dark conditions. Table 3 compiles and compares recorded device properties such as series resistance, ideality factor, barrier height, and rectification ratios using two independent models. Initially, the operational current shows a gradual increase before escalating rapidly due to the diffusion current in the Schottky diode. Furthermore, the substantial series resistance of the films and the existence of space charge limited current significantly influence the device's performance. Figure 8 depicts the reverse leakage current of Schottky diodes with values ranging from  $10^{-8}$  A to  $10^{-12}$  A. The notable decrease in leakage current by four orders of magnitude in the  $400^\circ\text{C}$  annealed film might stem from an increased concentration of  $\text{Cu}^{2+}$  states. Schottky

**Table 3** Comparison of the Schottky diode parameters using the Thermionic emission and Cheung model

Sample	Thermionic emission model		Cheung model			
	$\eta$	$\phi_B$ (eV)	$\eta$	$\phi_B$ (eV)	$R_s$ (from $dV/d(\ln I)$ vs I plot) K-ohm	$R_s$ (from $H(I)$ vs I plot) K-ohm
C RT	9.53	0.57	8.81	0.84	678	730
C 100	7.84	0.67	8.82	1.07	468	478
C 200	4.84	0.67	8.08	1.01	201	211
C 300	3.58	0.68	6.79	1.12	153	160
C 400	5.91	0.69	6.74	1.11	244	236
C 500	6.98	0.61	5.33	0.98	290	319

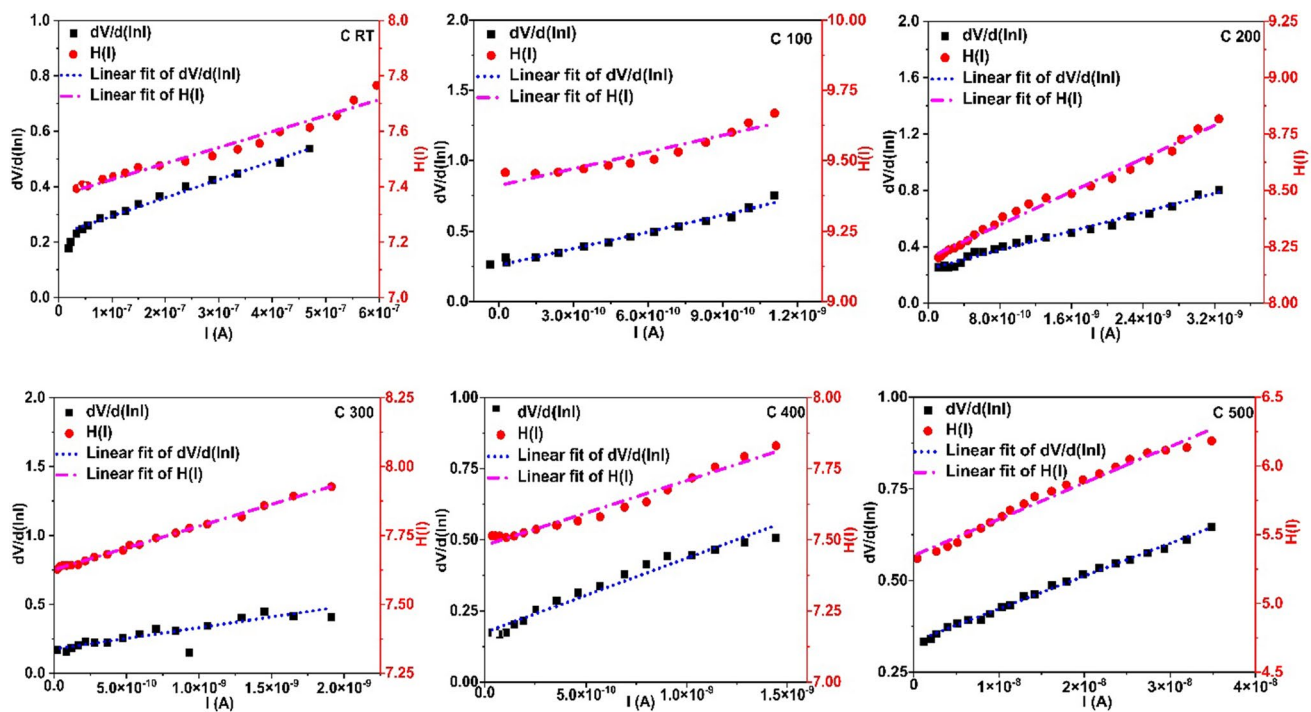


**Fig. 9** Representing the  $dV/d(\ln I)$  and  $H(I)$  versus  $I(A)$  plots for p-CuO/Al Schottky diode at different annealed temperatures

diodes created with active layers annealed at lower temperatures exhibited higher ideality factors alongside lower Schottky barrier heights. Conversely, in samples annealed at higher temperatures, substantial alterations occurred in both physical and chemical properties. This led to the creation of a more favorable barrier height for carriers to overcome, resulting in reduced leakage current and higher ideality factors. Additionally, higher ideality factor values indicate a departure from the TE (thermionic emission) theory regarding the current mechanism. The computed ideality factor from both the thermionic and Cheung models exceeded unity, which might be attributed to the presence of defect traps or interface states inside the films. Additionally, we noted a marginal rise in the Schottky barrier height, from 0.57 eV to 0.69 eV based on the TE model, and from 0.84 eV to 1.12 eV according to the Cheung model, as the annealing temperatures increased. Interestingly, at room temperature, the fabricated Schottky diode showcased a notably high ideality factor alongside a relatively modest barrier height. Deconvolution of the XPS O1s spectra reveals the presence of absorbed oxygen elements and a minor amount of O–H groups. These components might potentially contribute to the ITO/p-CuO/Al Schottky diode interface. Changes in barrier height and ideality factor caused by post-annealing treatments could also be attributed to increased surface roughness in the film, variations in its chemical composition, undesirable material interdiffusion, quantum mechanical tunneling effects, image force reduction, and the presence

of a thin insulating layer at the interface [2, 37]. The significant difference in parameters derived from the TE model and the Cheung model is primarily due to the existence of  $R_s$  and the existence of defect states. In this work, the obtained diode parameters like barrier height and  $R_s$  are better than the similar study done by Rajkumar Jana et al. [38].

Figure 10 illustrates the power law traits of the CuO/Al Schottky diodes. Determining whether the transport involves thermionic emission of holes or other means becomes challenging within a particular voltage range when the junction interface exhibits inhomogeneity. However, examining the power law characteristics allows for the identification of the predominant transport mechanism within that specific voltage range. A log  $I$  vs log  $V$  graph was drawn to depict the current conduction process. The relation  $I = AV^m$ , where  $m$  is the slope describing the type of the conduction mechanism and  $A$  is the arbitrary constant, was used to assess the three unique slopes on the plot. A dotted line divides the applied voltage ranges, separating them into three distinct regions. In region-I, characterized by a slope  $m$  approximately around 1 (ranging from 0.8 to 1.4), the conduction is attributed to the limited charges trapped, indicating that the transport mechanism is primarily governed by the thermionic emission of holes, prevailing over the Schottky barrier height [39, 40]. Similarly, the slopes in area II lie between 2 and 3, which may be described by the super quadratic behavior generated by low charge carrier concentrations. The phenomenon might be explained by the existence of traps inside metal

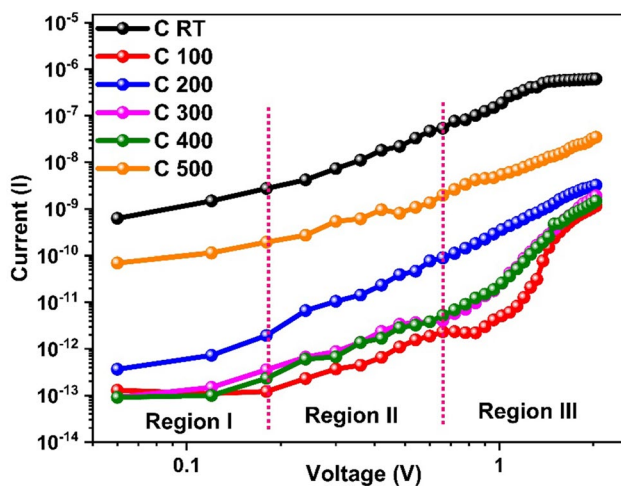


**Fig. 10** I–V (log scale) plot for space charge region

oxide films. This is because the metal oxide thin film layers are not formed on substrates with perfect epitaxial matching, which might result in traps that spread over the band-gap [35]. The mechanism of carriers escaping from traps owing to high carrier injection is explained in Region III, which has a slope larger than 3. This behavior contributes significantly to the phenomena known as space charge limiting current (SCLC). Space charge limited current (SCLC) emerges when all traps are completely occupied, and the quasi-static Fermi level precisely aligns with the energy of the shallow trap, causing a sudden surge in current. Therefore, we've concluded that space charge limited conduction (SCLC) takes precedence over both thermionic holes and the Schottky barrier height [39, 40]. Hence, the entirety of the conduction mechanism arises from barrier inhomogeneity, deviating from the TE (thermionic emission) model.

## 4 Conclusion

To summarize, the p-CuO/Al Schottky diodes were fabricated and characterized. A detailed analysis of its structural, chemical, morphological properties, and its transport characteristics has been carried out. Special attention has been paid to the effects of post-annealing treatment. When the annealing temperature was increased from 100 °C to 500 °C, the paramelaconite ( $\text{Cu}_4\text{O}_3$ ) phase of the copper oxide transformed to the cupric oxide (CuO) phase. The XRD study revealed that the film's crystallinity significantly decreased from 18.0 nm to 7.4 nm with a shift from  $\text{Cu}_4\text{O}_3$  to CuO phase. Raman spectroscopy findings demonstrated that the tenorite phase existed in high-temperature annealed films. In addition to the  $\text{Cu}^{2+}$  state, the  $\text{Cu}^+$  state was also represented by peaks in the XPS study. The paramelaconite phase is verified by the Cu: O ratio of 1.5:1. It is worth noting that

when the annealing temperature was raised, the samples' resistivity reduced, but their mobility and carrier concentration increased. Utilizing the thermionic emission and Cheung model, we observed an increase in barrier height with the escalating post-annealing process. The three orders of rectification were observed in a 400 °C annealed sample. The choice of annealing temperature with the combination of argon and oxygen ratio of metal oxide films could further enhance the diode parameters that will be beneficial for numerous applications including rectifiers, and switches in electronic circuits.

**Acknowledgements** The authors extend their appreciation to the Manipal Academy of Higher Education for their financial backing through the T M A Pai PhD Scholarship program. They also acknowledge RRCAT-Indore for granting access to the XPES-BL14 facility.

**Author contribution** DK: Conceptual ideas, supervision, and final version of the manuscript. JKA: Carried out the experiments, results analysis and draft copy of the manuscript.

**Funding** Open access funding provided by Manipal Academy of Higher Education, Manipal

**Data availability** The authors confirm that the data supporting the findings of this study are available within the document. The raw data that support the analysis of this study are available from the corresponding author, upon reasonable request.

## Declarations

**Conflict of interests** The authors verify that they have no disclosed financial or personal conflicts that could have impacted the research described in this study.

**Open Access** This article is licensed under a Creative Commons Attribution 4.0 International License, which permits use, sharing, adaptation, distribution and reproduction in any medium or format, as long as you give appropriate credit to the original author(s) and the source, provide a link to the Creative Commons licence, and indicate if changes were made. The images or other third party material in this article are included in the article's Creative Commons licence, unless indicated otherwise in a credit line to the material. If material is not included in the article's Creative Commons licence and your intended use is not permitted by statutory regulation or exceeds the permitted use, you will need to obtain permission directly from the copyright holder. To view a copy of this licence, visit <http://creativecommons.org/licenses/by/4.0/>.

## References

1. E. Guerrero, P.E. Rocha-Flores, G. Gutierrez-Heredia, N.A. Al-Ahmadi, *Mater. Res. Express* **7**, 032001 (2020)
2. S. Mao, T. Shang, B. Park, D. D. Anderson, S. J. Dillon, *Appl. Phys. Lett.* **104**, 153105 (2014)
3. P. Salunkhe, D. Kekuda, *J. Mater. Sci. Mater. Electron.* **33**, 21060 (2022)
4. B. Saha, K. Sarkar, A. Bera, K. Deb, R. Thapa, *Appl. Surf. Sci.* **418**, 328 (2017)
5. Z. Wang, P.K. Nayak, J.A. Caraveo-Frescas, H.N. Alshareef, *Adv. Mater.* **28**, 3831 (2016)



6. A. Yadav, A. Upadhyaya, S.K. Gupta, A.S. Verma, C.M.S. Negi, *Thin Solid Films* **675**, 128 (2019)
7. C. Dumitru, L. Fara, Ø. Nordseth, I. Chilibon, R. Kumar, B. G. Svensson, F. Dragan, V. Muscurel, D. Craciunescu, P. Sterian, *PVCon 2018—Int. Conf. Photovolt. Sci. Technol.* (2018)
8. E.M. Alkoy, P.J. Kelly, *Vacuum* **79**, 221 (2005)
9. L. Debbichi, M.C. Marco De Lucas, J.F. Pierson, P. Krüger, *J. Phys. Chem. C* **116**, 10232 (2012)
10. S. S. Shariffudin, S. S. Khalid, N. M. Sahat, M. S. P. Sarah, H. Hashim, *IOP Conf. Ser. Mater. Sci. Eng.* **99**, 012007 (2015)
11. A. Prakash, V.S. Ganesha Krishna, S.N. Moger, M.G. Mahesha, *Mater. Today Commun.* **32**, 103926 (2022)
12. M. Ozga, J. Kaszewski, A. Seweryn, P. Sybilski, M. Godlewski, B.S. Witkowski, *Mater. Sci. Semicond. Process.* **120**, 105279 (2020)
13. B. Purusottam-Reddy, K. Sivajee-Ganesh, K. Jayanth-Babu, O.M. Hussain, C.M. Julien, *Ionics (Kiel)*. **21**, 2319 (2015)
14. C.R. Gobbiner, G.R. Dillip, S.W. Joo, D. Kekuda, *Ceram. Int.* **44**, 16984 (2018)
15. L. Radjehi, L. Aissani, A. Djelloul, S. Lamri, K. Nomenyo, S. Achache, G. Lerondel, F. Sanchette, *Surf. Eng.* **37**, 422 (2021)
16. D.S. Murali, S. Aryasomayajula, *Appl. Phys. A* **124**, 279 (2018)
17. Y. J. Lin, J. Luo, H. C. Hung, *Appl. Phys. Lett.* **102**, 193511 (2013)
18. J. Ramírez-Ortiz, T. Ogura, J. Medina-Valtierra, S.E. Acosta-Ortiz, P. Bosch, J. Antonio De Los Reyes, V.H. Lara, *Appl. Surf. Sci.* **174**, 177 (2001)
19. J. Li, G. Vizkelethy, P. Revesz, J.W. Mayer, K.N. Tu, *J. Appl. Phys.* **69**, 1020 (1991)
20. V.S. Levitskii, V.I. Shapovalov, A.E. Komlev, A.V. Zav'yalov, V.V. Vit'ko, A.A. Komlev, E.S. Shutova, *Tech. Phys. Lett.* **41**, 1094 (2015)
21. S. Dolai, R. Dey, S. Das, S. Hussain, R. Bhar, A.K. Pal, *J. Alloys Compd.* **724**, 456 (2017)
22. J. C. Irwin, T. Wei, J. Chrzanowski, *Physica C*. **48**, 76 (1993)
23. J.Y. Park, T.H. Kwon, S.W. Koh, Y.C. Kang, *Bull. Korean Chem. Soc.* **32**, 1331 (2011)
24. S. Dolai, S. Das, S. Hussain, R. Bhar, A.K. Pal, *Vacuum* **141**, 296 (2017)
25. D. S. Kozak, R. A. Sergiienko, E. Shibata, A. Iizuka, T. Nakamura, *Sci. Rep.* **6**, 21178 (2016)
26. F.A. Akgul, G. Akgul, N. Yildirim, H.E. Unalan, R. Turan, *Mater. Chem. Phys.* **147**, 987 (2014)
27. J. Morales, L. Sánchez, F. Martín, J.R. Ramos-Barrado, M. Sánchez, *Thin Solid Films* **474**, 133 (2005)
28. M.A. Brisk, A.D. Baker, *J. Electron Spectros. Relat. Phenomena* **7**, 197 (1975)
29. M.C. Biesinger, *Surf. Interface Anal.* **49**, 1325 (2017)
30. K.J. Blobaum, D. Van Heerden, A.J. Wagner, D.H. Fairbrother, T.P. Weihs, *J. Mater. Res.* **18**, 1535 (2003)
31. Z.H. Gan, G.Q. Yu, B.K. Tay, C.M. Tan, Z.W. Zhao, Y.Q. Fu, *J. Phys. D Appl. Phys.* **37**, 81 (2004)
32. P. Salunkhe, A. V. Muhammed Ali, D. Kekuda, *Mater. Res. Express* **7**, 016427 (2020)
33. M. Jlassi, I. Sta, M. Hajji, B. Ben Haoua, H. Ezzaouia, *Mater. Sci. Semicond. Process.* **26**, 395 (2014)
34. H. Özerli, A. Bekereci, A. Türüt, Ş. Karataş, *J. Alloys Compd.* **75–84**, 718 (2017)
35. M. Tyagi, M. Tomar, V. Gupta, *Mater. Res. Bull.* **66**, 123 (2015)
36. Y.J. Lee, M.A. Schweitz, J.M. Oh, S.M. Koo, *Materials (Basel)*. **13**, 434 (2020)
37. U. Parihar, J. Ray, C.J. Panchal, N. Padha, *Appl. Phys. A Mater. Sci. Process.* **122**, 1 (2016)
38. R. Jana, S. Sil, A. Dey, J. Datta, P. P. Ray, *AIP Adv.* **8**, 125104 (2018)
39. F. Yakuphanoglu, N. Tugluoglu, S. Karadeniz, *Phys. B* **392**, 188 (2007)
40. Ç. Bilkan, S. Zeyrek, S. E. San, Ş. Altındal, *Mater. Sci. Semicond. Process.* **137–144**, 32 (2015)

**Publisher's Note** Springer Nature remains neutral with regard to jurisdictional claims in published maps and institutional affiliations.